Paper: ASAT-13-MO-21

13th International Conference on
AEROSPACE SCIENCES & AVIATION TECHNOLOGY,
ASAT- 13, May 26 – 28, 2009, E-Mail: asat@mtc.edu.eg
Military Technical College, Kobry Elkobbah, Cairo, Egypt
Tel : +(202) 24025292 – 24036138, Fax: +(202) 22621908

High Speed Inlet Stage for an Advanced High-Pressure Ratio Core Compressor: Numerical Flow Field Prediction and Verification

Mohamed K. Khalil* , MA Hongwei**

Abstract: NASA rotor 37 is among the most popular rotors that have been manufactured to date. It was designed and tested in early 1980's by Reid and Moore at NASA Glenn Research Center. It consists of 36 blades with multiple arc profiles, and was designed for compressors with compression ratio of 2.05 at mass flow rate of 20.19 kg/s. Also, it was tested in isolation with circumferentially uniform inlet flow so that the flow through it should be steady apart from any effects of passage to passage geometry variation, and mechanical vibration. As such it represents the simplest possible type of test for a real challenge to 3D viscous flow solvers because chock wave-boundary layer interaction is strong and the effects of viscosity are dominate in determining flow deviation and hence pressure ratio. Computational fluid dynamics (CFD) predictions were obtained by ANSYS-CFX 11.0 with k-ε turbulence model, and were compared with experimental data which has been taken by NASA. The code predictions (with a uniform and spanwise varying outlet static pressure) show good agreement with respect to measured overall performance characteristic, averaged pitchwise distributions, and averaged spanwise distributions. So, the code now is verified to use with the turbulence model, for farther calculation of turbomachinery. Specially, compressors, compressors blades, and compressors cascade.

Keywords: Transonic compressor rotor, Computational fluid dynamics solutions, Rotor 37.

Nomenclature

M = Mach number
$\dot{m}$ = mass flow rate
P = pressure / static pressure
T = temperature

Subscripts

* = total conditions
out = outlet
chock = calculated chocking conditions
rel = relative

* PhD Candidate, Beijing University for Aeronautics and Astronautics, khilo99@yahoo.com.
** Professor, Beijing University for Aeronautics and Astronautics, mahw@buaa.edu.cn

Introduction

Turbomachinery blades are usually designed with proprietary design codes and are heavily analyzed with CFD codes before committing to manufacture. However, the turbomachinery designers often distrust absolute performance predictions and rely only on changes in predicted performance between designs. This practice suggests that the accuracy of CFD codes can still be improved. In 1992 the turbomachinery committee of the International Gas Turbine Institute (IGTI), also in 1993 the Turbomachinery Committee of (ASME) issued an invitation for CFD calculations on test case concerning a transonic axial compressor rotor to compare the calculations with detailed experimental results, NASA (Lewis Research Center) offered a suitable test case in the form of a highly loaded transonic compressor rotor which was then being tested with extensive use of a laser anemometry to measure the internal flow.

The purpose of the exercise was to provide a forum for a careful assessment of the ability of turbomachinery CFD codes to predict the overall performance and the flow field in a modern axial blading over a range of operating conditions. The test compressor, designed as NASA stage 37, was designed by the NASA Lewis Research Center as an inlet stage for a core compressor of an aircraft engine. For the code assessment exercise the rotor was tested in isolation to avoid any interaction from upstream inlet guide vanes or downstream stator blades. The rotor design pressure ratio is 2.11 at mass flow rate of 20.19 kg/s. The inlet relative Mach number is 1.13 at hub and 1.48 at tip at design tip speed of 454.14 m/s. The rotor aspect ratio is 1.19 and the hub / tip radius ratio is 0.70. The rotor tip clearance at the design speed is approximate 0.40 mm corresponding to 0.5% of inlet span and 0.7% of the exit span [1]. The measurements were performed in the single stage transonic test facility at the NASA Lewis Research Center using aerodynamic probes and a laser anemometry.

Test Case Details

Full details of the test case geometry are available from NASA Lewis. A meridional view of the flow path is shown in Fig. 1. The aerodynamic designs parameters are given by Reid & Moore (1978) and are summarized below in Table 1. The detailed laser surveys of the flow field are available at stations 2 and 3. An aerodynamic probe traverse data, with a temperature probe traverse data, and the area change at stations 1 and 4 were processed to obtain the compressor pressure ratio, the mass flow, the efficiency, and the mass flow rate characteristic. The inlet distributions of stagnation pressure and the temperature were provided to predict overall performance and to present predictions of detailed flow field at points corresponding to 98% and 92% of their own calculated chocking flow rate. Because previous studies have shown that the calculated pressure ratio and the efficiency depend significantly on the method by which flow field is averaged, it was requested that the calculated results should be averaged in the same way as the experimental data to compare the overall performance.

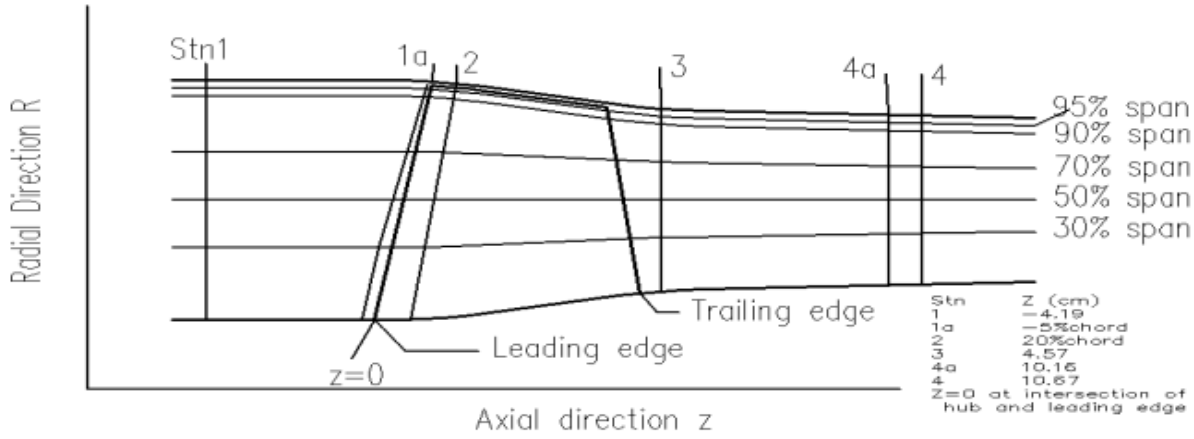

Fig. 1 Meridional channel and measurement planes of NASA rotor 37

Table 1 Aerodynamic design parameters

Number of blades	36
Tip diameter at leading edge	0.5074 m
Hub diameter at leading edge	0.3576 m
Rotational speed (corrected)	17188.7 rpm
Tip solidity	1.288
Tip clearance	0.356 mm
Tip speed	454.14 m/s
Pressure ratio	2.106
Mass flow rate (corrected)	20.19 kg/s
Blading	Multiple Circular Arcs

Purpose of Calculations

The objective of calculations is to prove the accuracy of ANSYS-CFX results and solve the exercise with acceptable computational time, so go farther calculations. The computational grids are 483272 nods, leading to CPU times between 2 and 6 hours per run, in a normal PC with core 2 duo processor, and 2 GB RAM. Furthermore it was necessary to define the geometry and the boundary conditions with reasonable simplifications. It is of the great importance to industrial users to find out code was capable of achieving good results on a very specialized turbomachinery problem. ANSYS-CFX 11.0 has been used without any modifications to the flow solver or turbulence model. The flow field was calculated in the rotating frame of reference and was considered as steady state.

Code used and Grids

The commercial code ANSYS-CFX 11.0 supplied from ANSYS, Inc., PA, USA. It is for widely used for internal flow and especially turbomachinery blading. ANSYS-CFX takes advantage of data and information common to many simulations. This begins with common geometry; Users can link to existing native computer-aided design (CAD) packages as well as create and / or modify the CAD models in an intuitive solid modeling environment. Complementing common geometry model is a suite of meshing tools, designed to ensure easy generation of the most appropriate mesh for the given application. ANSYS-CFX tools then

guide the user through the setup of operating conditions, the selection of materials and the definition of models. The ANSYS-CFX solver uses the most modern solution technology with a coupled algebraic multi-grid solver, farther more, the extremely efficient parallelization to help ensure that solutions are ready for analysis quickly and reliably. Solution analysis with the ANSYS-CFX post-processor gives users power to extract any desired quantitative data from the solution; the ANSYS-CFX post-processor also provides comprehensive set of flow visualization options. Animations of flow simulations are easily generated, and 3D images can be directly created and shared. It can handle incompressible as well as compressible flows. ANSYS-CFX includes the following features:

- An advanced coupled solver that is both reliable and robust.

- Full integration of problem definition, analysis, and results presentation.

- An intuitive and interactive setup process, using menus and advanced graphics.

It can solve the 3D Navier-Stokes, mass, and the energy equations in stationary or rotating frames of reference. The viscous effects are simulated by k-ε turbulence model. The J-grid mesh topology is used in the calculation, while An O-grid topology is used around the blade with 0.3 width factor. The total grid consists of 483272 nodes and 447140 elements. Fig. 28. shows mesh topology in meridional plane.

Boundary Conditions

Axial inlet flow in absolute system was specified over the entire inlet face, the total pressure (P*) and total temperature (T*) were used. The static outlet pressure was specified on hub at outlet and varied to achieve the mass flow rate as part of the solution. Axial inlet flow direction in the absolute system as well as the constant absolute total pressure and the temperature were specified over the entire inlet face. Although the prescribed experimental total pressure distribution shows slight non-uniformities due to the boundary layers.

Comparison of Overall Performance

The overall aerodynamic performance of Rotor 37 was obtained. The chocking mass flow is a good measure of the accuracy of the inviscid part of the solution because the boundary layer blockage at the throat is extremely small and so the chocking mass flow is determined by the geometrical throat area. Mass flow rates as close as possible to 98% and 92% of the chock mass flow rates which is 20.93 kg/s. So, the first step in calculation was to determine the chock mass flow rates. Lower mass flow is very near to the stall limit which was measured at 19.23 kg/s. the solution presented at $\dot{m}$ = 18.679 kg/s (P_{out} = 137325 Pa) is a converged solution for a calculations of 200 steps, but the flow rate was not stable and slightly dropping when used 400 steps instead of 200 steps calculations, which were normally used to confirmed this trend. On the other hand, a slightly lower outlet static pressure led to a stable solution at $\dot{m}$ = 19.15 kg/s (P_{out} = 136325 Pa). Calculations the stall limit could be accurately identified, which corresponding to the lower pressure ratio (around 1.00). This value was found to be $\dot{m}$ = 20.989 kg/s, which is very close to the measured value. Fig. 2 compares total pressure ratio and mass flow rate characteristic measured with the predicted values. It also shows the variations of efficiency with mass flow rate.

Figure 3 shows comparison between measured and predicted data of total temperature ratio with a good agreement. The interesting point about the characteristic is that the peak

efficiency is reached at a few percent lower than chocking mass flow rate. The reason for this is that near chock the chock system in the inner half of rotor 37 consists of two distinct chocks, a bow chock and a passage chock. At lower mass flow rates these chocks combine to form a single strong bow chock. The fact is that the compression is split between two chocks at low pressure ratios which reduces the chock loss and so increase the efficiency. The reason why this occurs in rotor 37 is believed that the relatively thick blade sections cause a large leading edge wedge angle which in turn produces a strong bow chock. This is a desirable feature which should be encouraged in design when possible [2].

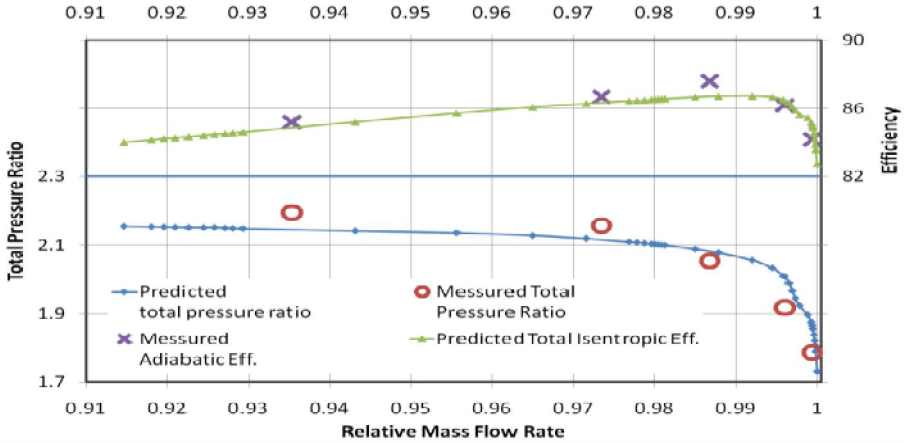

Fig. 2 The total pressure ratio and efficiency measured and predicted.

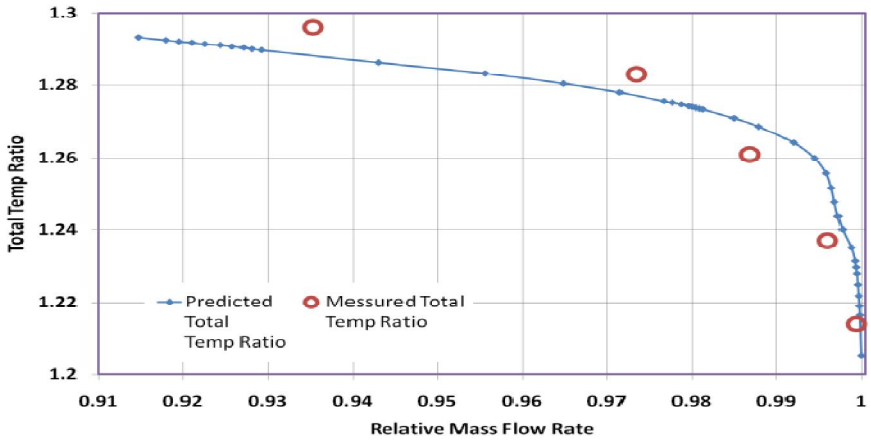

Fig. 3 Total temperature ratio

Results

The comparisons of measured and predicted data at the 98% and 92% of chock mass flow rate at station 4 are obtained and calculated, Fig. 4 and Fig. 5 show spanwise distribution of total pressure ratio at different mass flow conditions, while Fig. 6 and Fig. 7 show the spanwise distribution of total temperature ratio. Curves show good agreement between measured and predicted data. Absolute flow angle at 98% and 92% of chock mass flow rate are shown respectively in Fig. 8 and Fig. 9. Small difference between the measured and predicted data of absolute flow angle is due to the stronger tip leakage flow, while Fig.10 and Fig. 11 show the spanwise distribution of the normalized tangential velocity at 98% and 92% of chock mass flow rate.

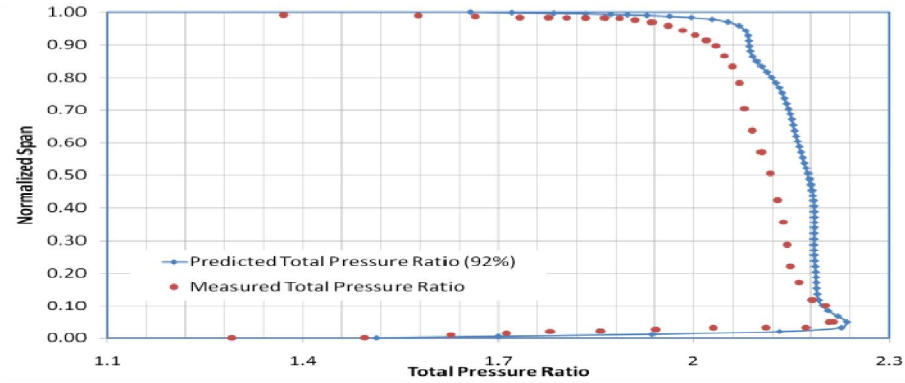

Fig. 4 Spanwise distribution of total pressure ratio at $\dot{m}/\dot{m}_{chock} = 0.92$

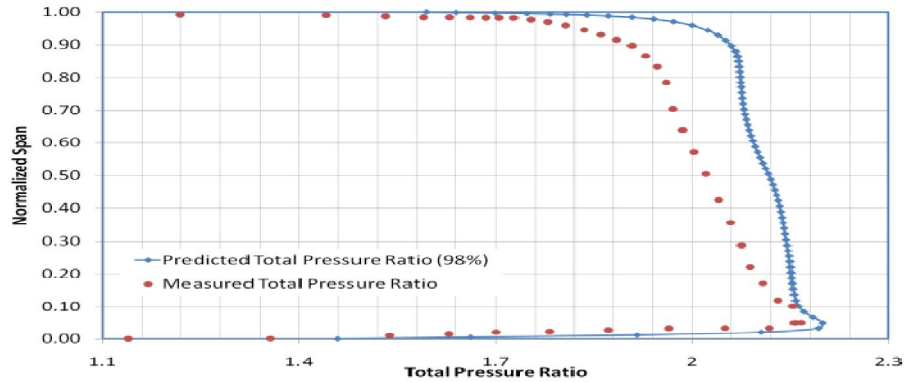

Fig. 5 Spanwise distribution of total pressure ratio at $\dot{m}/\dot{m}_{chock} = 0.98$

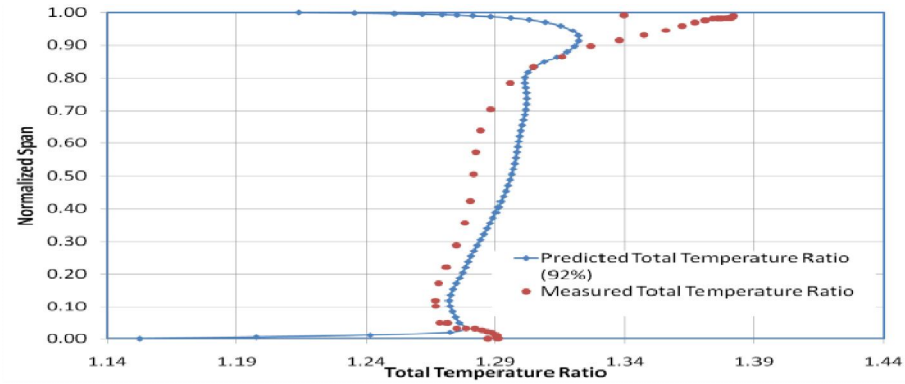

Fig. 6 Spanwise distribution of total temperature ratio at $\dot{m}/\dot{m}_{chock} = 0.92$

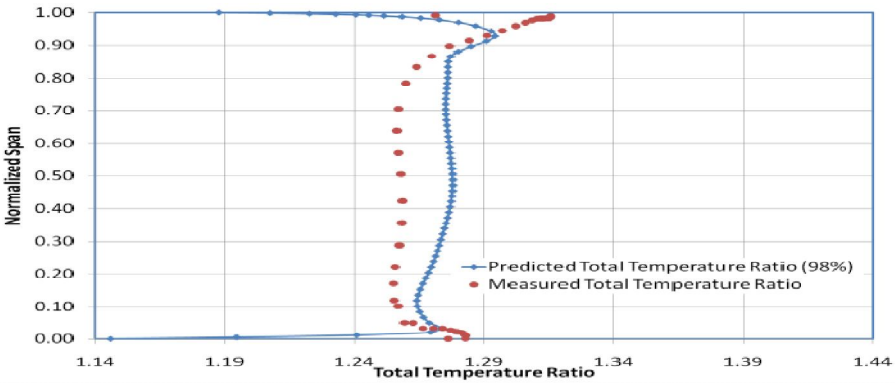

Fig. 7 Spanwise distribution of total temperature ratio at $\frac{\dot{m}}{\dot{m}_{chock}} = 0.98$

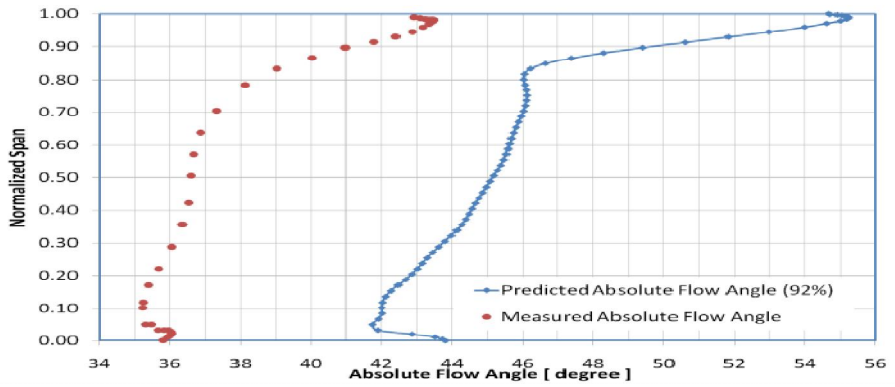

Fig. 8 Spanwise distribution of absolute flow angle at $\frac{\dot{m}}{\dot{m}_{chock}} = 0.92$

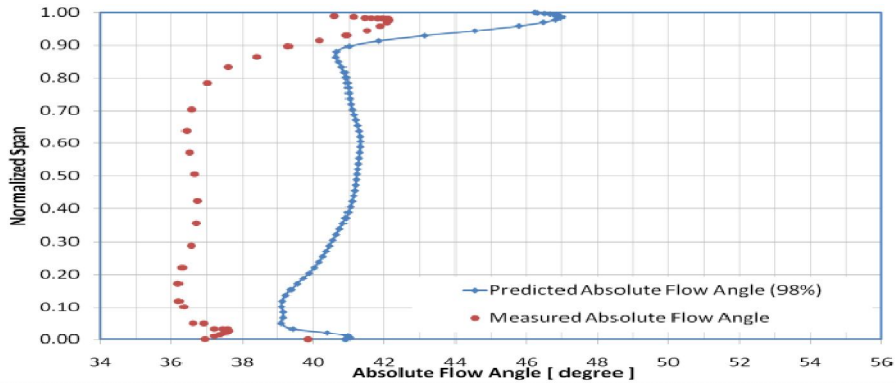

Fig. 9 Spanwise distribution of absolute flow angle at $\dot{m}/\dot{m}_{chock} = 0.98$

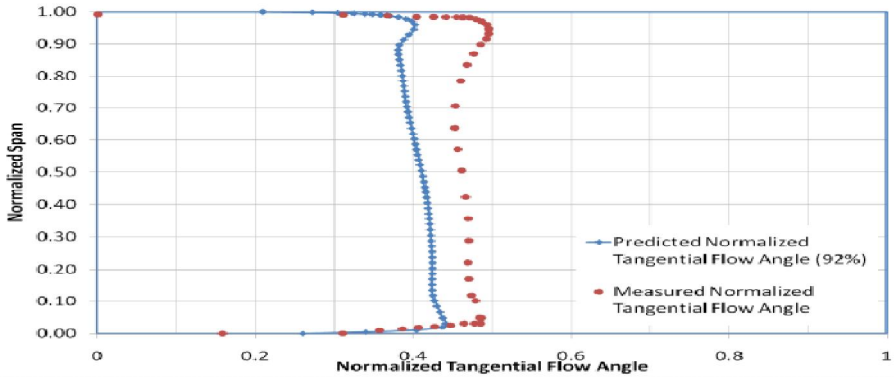

Fig. 10 Spanwise distribution of normalized tangential velocity at $\dot{m}/\dot{m}_{chock} = 0.92$

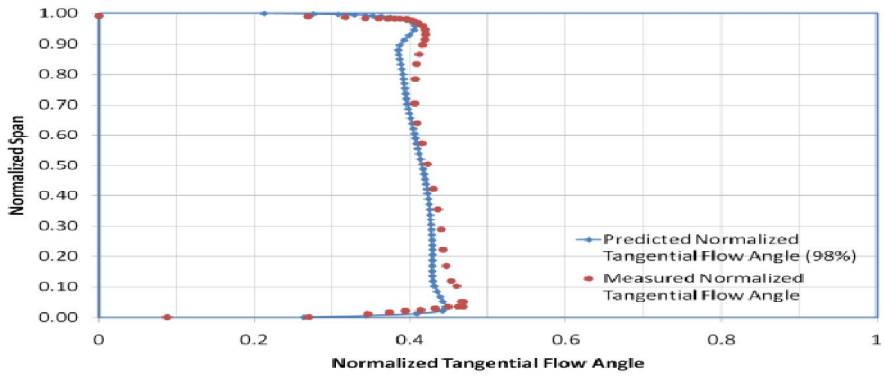

Fig. 11 Spanwise distribution of normalized tangential velocity at $\dot{m}/\dot{m}_{chock} = 0.98$

The good predicted of wake at 98% and 92% of the chock mass flow rate with respect to experiment in near to wall region (station 3) is shown in Fig. 12 to Fig. 17 at 50%, 90%, and 95% span respectively. Downstream of trailing edge near the blade tip, a strong interaction between the tip leakage vortex, the shroud boundary layer and the blade wake take place.

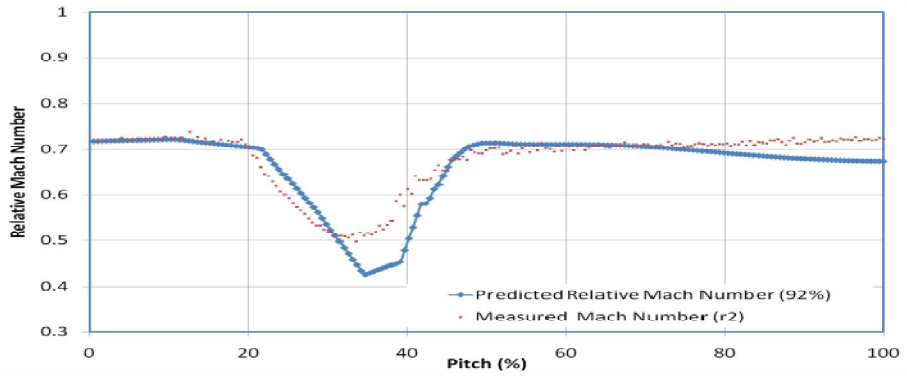

Fig. 12 Pitchwise distribution of relative mach number at $\dot{m}/\dot{m}_{chock} = 0.92$ at station 3, 50% span

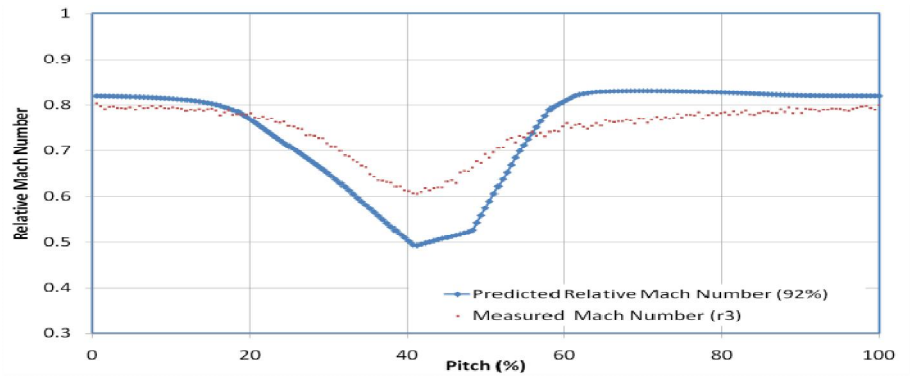

Fig. 13 Pitchwise distribution of relative mach number at $\dot{m}/\dot{m}_{chock} = 0.92$ at station 3, 90% span

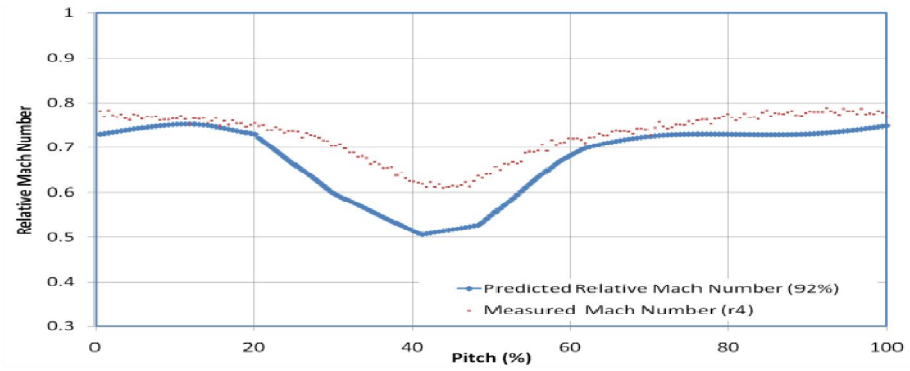

Fig. 14 Pitchwise distribution of relative mach number at $\dot{m}/\dot{m}_{chock} = 0.92$ at station 3, 95% span

Also, the figures show that the axial distance traveled by a fluid particle from blade trailing edge plane to exit is more than the axial distance of the periodic planes. All phenomena are confirmed in, where measured and predicted relative Mach number contours at 50%, 90%, and 95% span are compared at the 92% and 98% of chock mass flow rate.

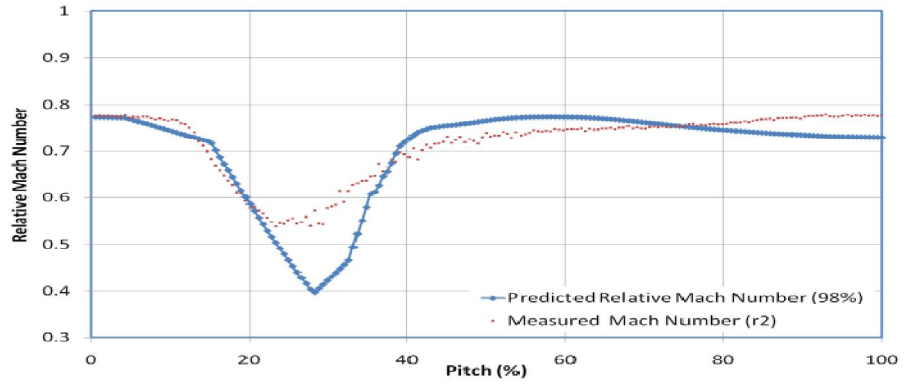

Fig. 15 Pitchwise distribution of relative mach number at $\dot{m}/\dot{m}_{chock} = 0.98$ at station 3, 50% span

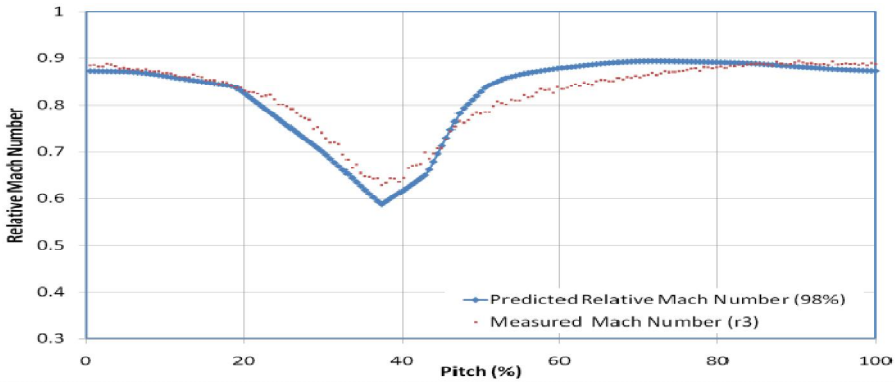

Fig. 16 Pitchwise distribution of relative mach number at $\dot{m}/\dot{m}_{chock} = 0.98$ at station 3, 90% span

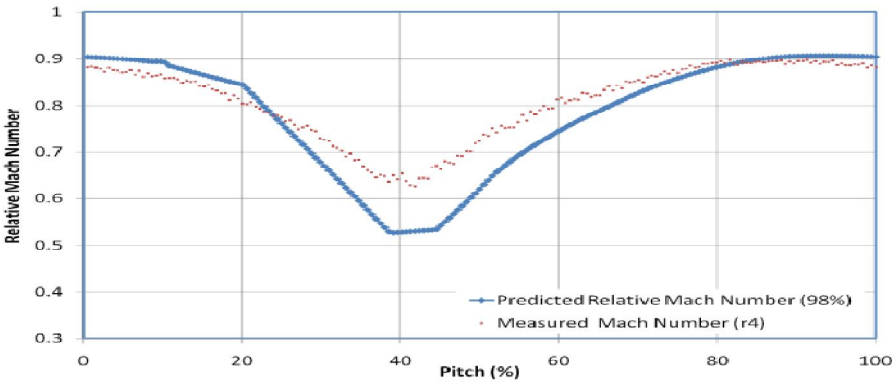

Fig. 17 Pitchwise distribution of relative mach number at $\dot{m}/\dot{m}_{chock} = 0.98$ at station 3, 95% span

A very important feature of Mach number contours is that the post chock Mach numbers are generally predicted to be significantly lower than measured. This is difficult to verify from the contours but is better illustrated in Fig. 18 to Fig. 20 at 92% of chock mass flow rate, while Fig. 21 to Fig. 23 at 98% of chock mass flow rate which shows the pitchwise variation of Mach number through the chock at station 2 for 50%, 90%, and 95% span respectively. Unfortunately the laser data does not extend to suction surface but it is clear that the predicted Mach numbers agree well with the measured ones in front of the chock but almost all predictions are too low after the chock. This is the key of over prediction of pressure ratio and most likely explanation is that the increase in the boundary layer interaction is actually greater than predictions.

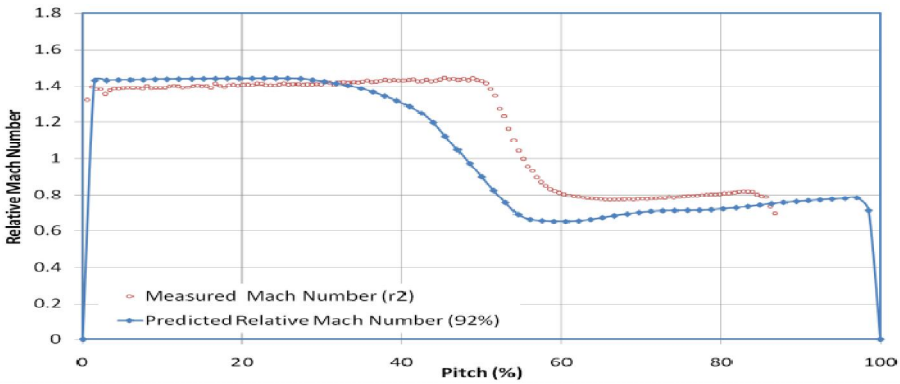

Fig. 18 Pitchwise distribution of relative mach number at $\dot{m}/\dot{m}_{chock} = 0.92$ at station 2, 50% span

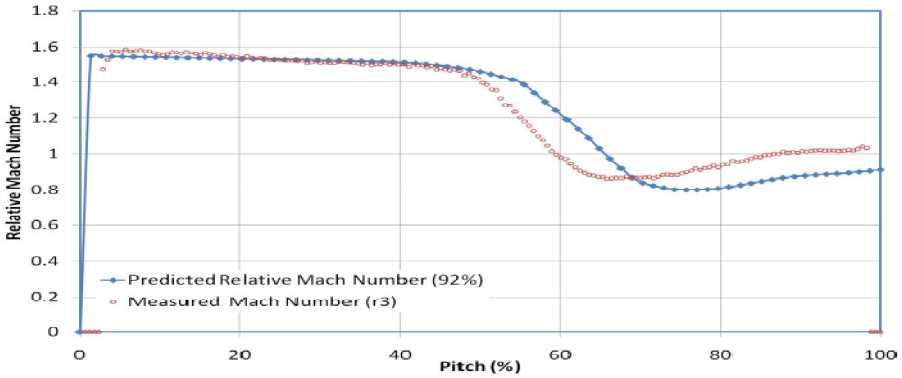

Fig. 19 Pitchwise distribution of relative mach number at $\dot{m}/\dot{m}_{chock} = 0.92$ at station 2, 90% span

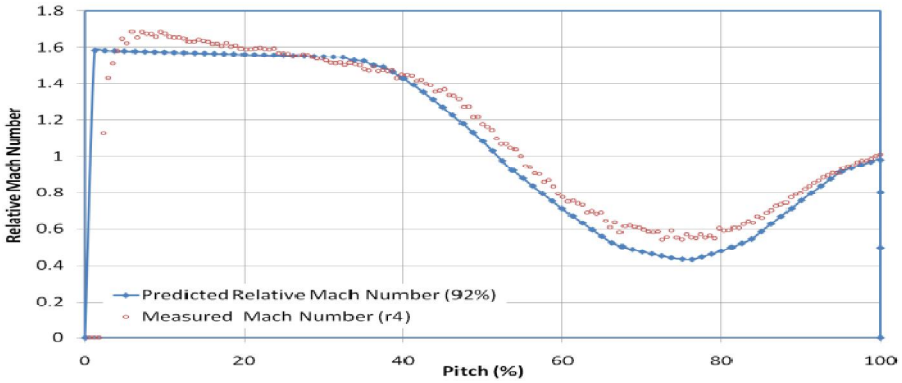

Fig. 20 Pitchwise distribution of relative mach number at $\dot{m}/\dot{m}_{chock} = 0.92$ at station 2, 95% span

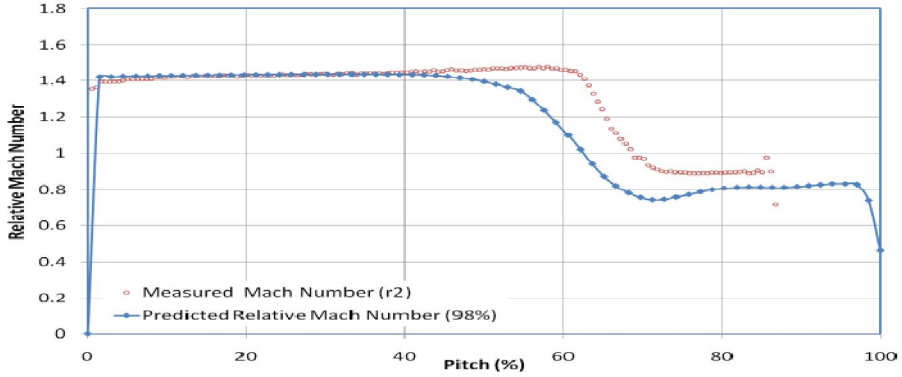

Fig. 21 Pitchwise distribution of relative mach number at $\dot{m}/\dot{m}_{chock} = 0.98$ at station 2, 50% span

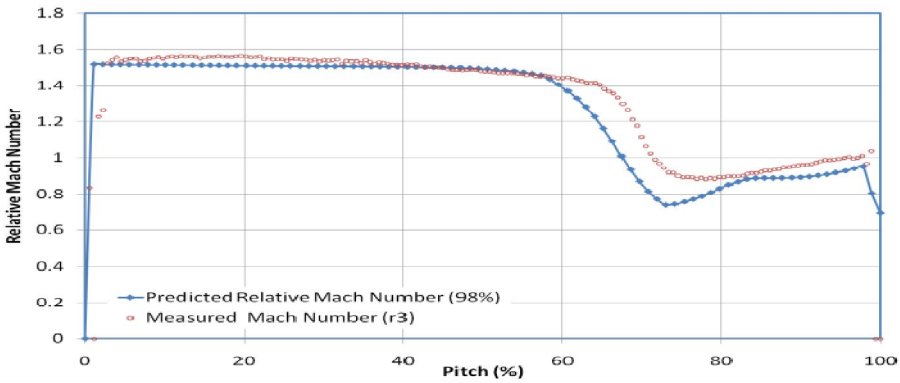

Fig. 22 Pitchwise distribution of relative mach number at $\dot{m}/\dot{m}_{chock} = 0.98$ at station 2, 90% span

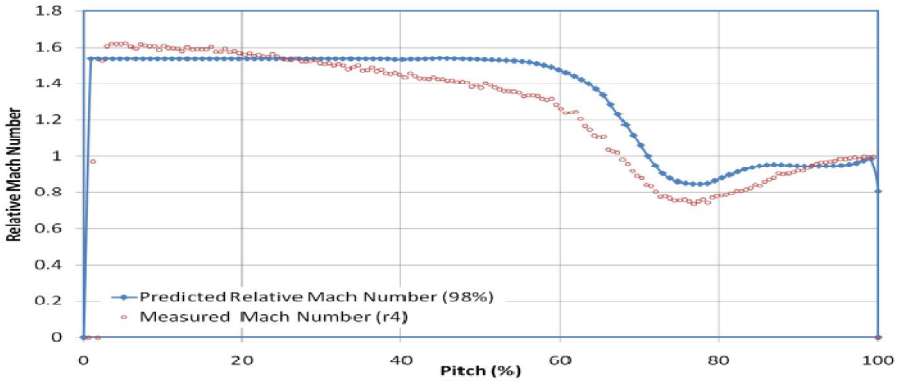

Fig. 23 Pitchwise distribution of relative mach number at $\dot{m}/\dot{m}_{chock} = 0.98$ at station 2, 95% span

Conclusions

Flow filed calculation with the code have been presented and compared with measurements of NASA transonic compressor rotor 37. Code's results show generally very good agreement with the measurements. The results can be summarized as follows:

- The code shows very good predictions of overall values, the average pitchwise, and the average spanwise distributions.

- In general, the efficiency is predicted to within ±0.4%. Also, the overall shapes of the characteristics are estimated reasonably well.

- The k-ε turbulence model displays very good predictions of certain local details of the flow field, especially near the tip clearance and wakes.

- The code demonstrates that the distribution of pressure prescribed at the exit boundary has a considerable influence on the axial velocity and flow angle distributions in the exit region only, but not on the rest of the flow field.

- An important conclusion of this work is the turbomachinery CFD blade row calculations can achieve very good levels of accuracy when used with about 480000 nodes.

- The ANSYS-CFX is proved to use for future work especially compressors.

Acknowledgement

This work was funded by the Chinese Key Laboratory Fund, (Grant No. 914 0C3 310 040 705), the National Science Foundation of China, (Grant No. 50776004), supported by the 111 Project, No. B07009.

References

[1] Reid L. and Moore R.D., "Design and overall performance of four high – speed inlet stages for an advanced high – pressure - ratio core compressor", 1978, NASA, TP 1337.

[2] Denton, J. D., ''Lessons Learned From Rotor 37'', Sept. 1–6, 1996, 3rd ISAIF, Beijing, China.

[3] Razvan Mahu, and Cristina Oprea, "Compressors benefit from NASA rotor 37", 2006, Aerospace, fluent news.

[4] Reid L. and Moore R.D., "Performance of single stage axial flow compressor with rotor and stator aspect ratios of 1.19 and 1.26 respectively, and with a design pressure ratio of 2.05", 1980, NASA, TP 1659.

[5] Wisler D. C., ''Loss Reduction in Axial Flow Compressors through Low-Speed Model Testing'', 1985, ASME Jet Turbo-machinery (JTM), pp. 354–363.

[6] Adamczyk, J. J., Celestina, M. L., and Greitzer, E. M., "The Role of Tip Clearance in High-Speed Fan Stall'', 1993, ASME (JTM), 115, pp. 28–38.

[7] Dawes, W. N., ''A Numerical Analysis of the Three-Dimensional Viscous Flow in a Transonic Compressor Rotor and Comparison with Experiment'', 1987, ASME (JTM), 109, pp. 83–90.

[8] Dunham, J., "An AGARD Working Group Study of 3D Navier–Stokes Codes Applied to Single TM Blade Rows'', ASME, 98-GT-50.

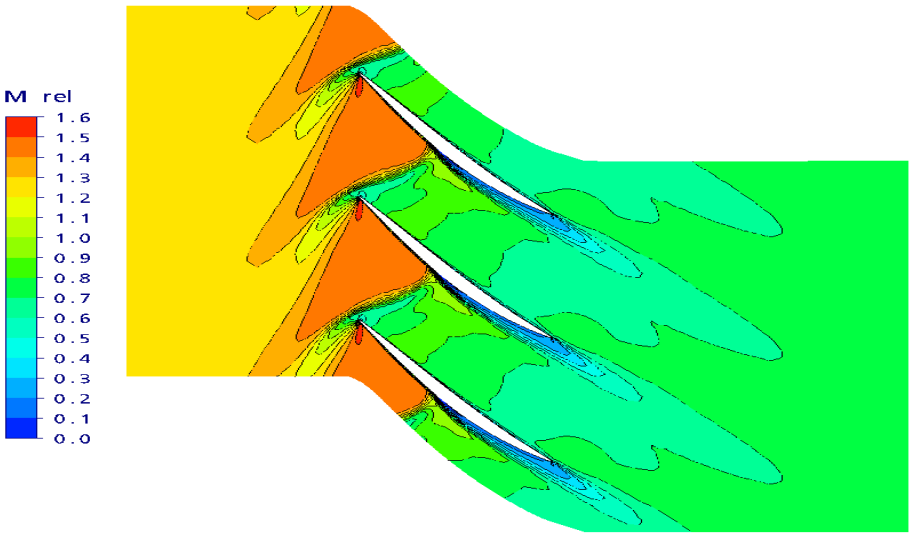

Fig. 24 M_{rel} 50% span at $\dot{m}/\dot{m}_{shock} = 0.92$

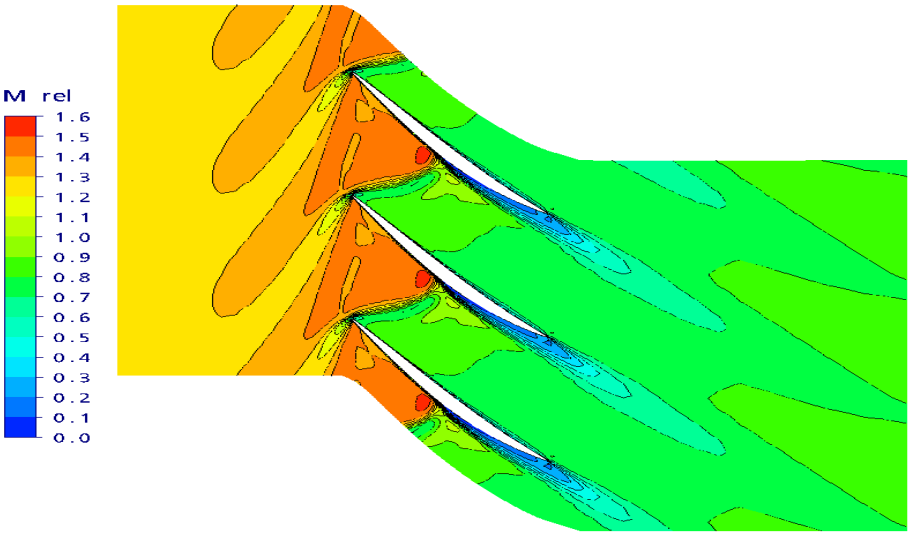

Fig. 25 M_{rel} 50% span at $\dot{m}/\dot{m}_{shock} = 0.98$

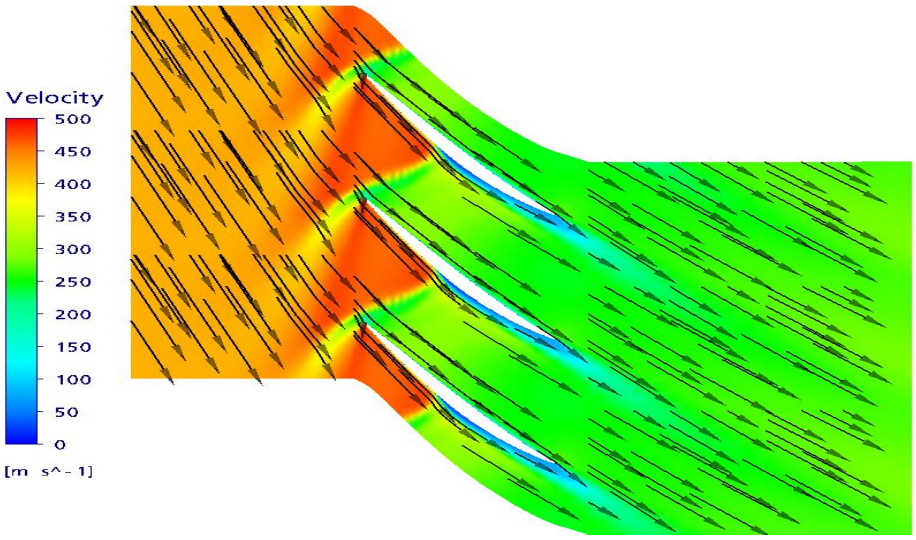

Fig. 26 Velocity vector 50% span at $\dot{m}/\dot{m}_{shock} = 0.92$

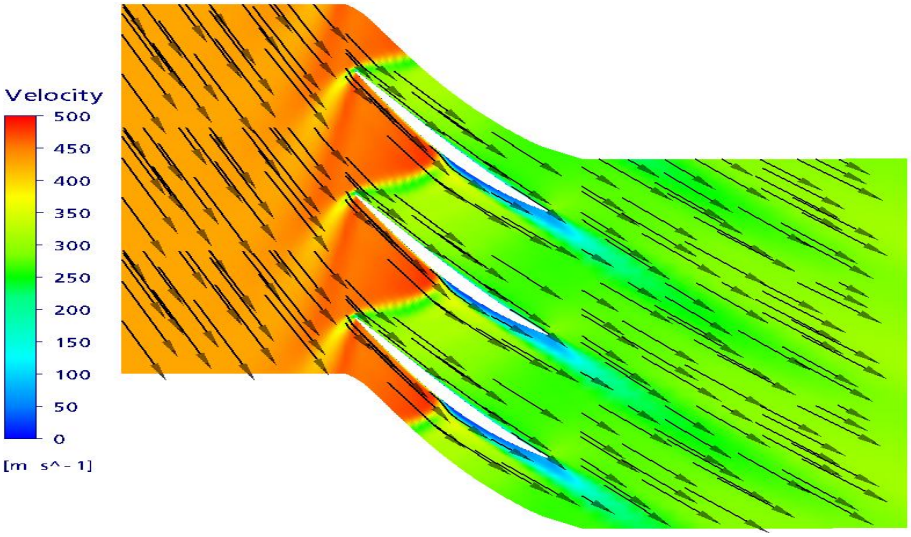

Fig. 27 Velocity vector 50% span at $\dot{m}/\dot{m}_{shock} = 0.98$

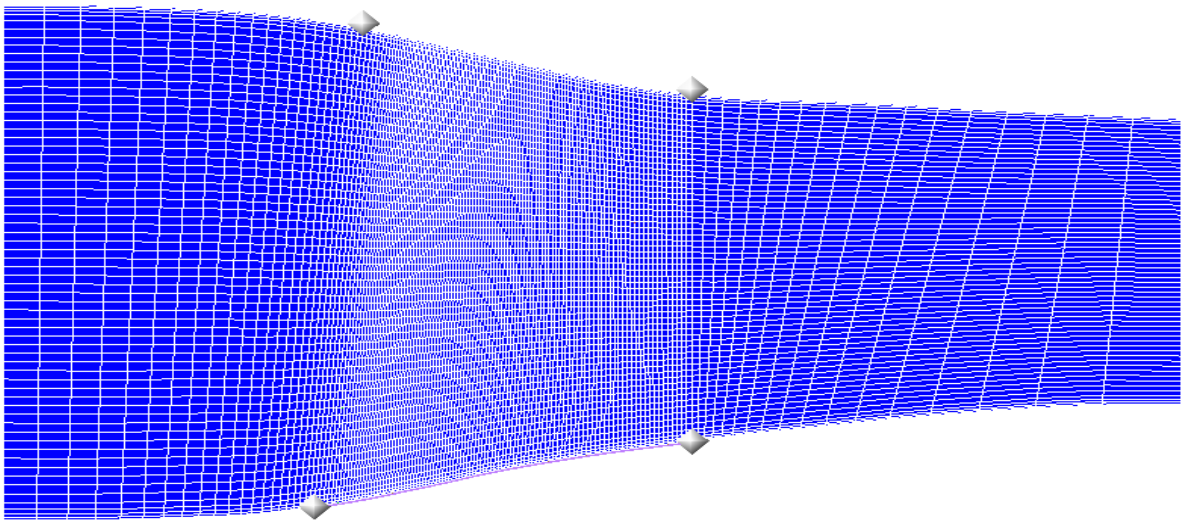

Fig. 28 Meridional plane mesh